minerals

MDPI

Article

Partial Melting of Lithospheric Mantle and Formation of the Early Cretaceous Alkaline Rocks in the Guandimiao REE Deposit, Luxi Terrane, Eastern China

Ze-Chen Xi [1,2], Kun-Feng Qiu [1,2,*], Cheng-Long Zhi [1,2,*], Shan-Shan Li [1], Zhen Shang [2] and Ya-Qi Huang [1,3]

[1] State Key Laboratory of Geological Processes and Mineral Resources, School of Earth Sciences and Resources, China University of Geosciences, Beijing 100083, China; zechenxi10@163.com (Z.-C.X.); lishanshan199811@163.com (S.-S.L.); hyaq_1014@163.com (Y.-Q.H.)
[2] Shandong Provincial Lunan Geology and Exploration Institute (Shandong Provincial Bureau of Geology and Mineral Resources No.2 Geological Brigade), Jining 272100, China; shangxiaohuai@yeah.net
[3] MNR Key Laboratory of Metallogeny and Mineral Assessment, Institute of Mineral Resources, Chinese Academy of Geological Sciences (CAGS), Beijing 100037, China
* Correspondence: kunfengqiu@cugb.edu.cn (K.-F.Q.); 13853768183@163.com (C.-L.Z.)

Abstract: The Luxi Terrane (eastern China) exposes widespread Early Cretaceous alkaline rocks, whereas their petrogenesis remains controversial, including fractional crystallization, partial melting and crustal contamination regime. Here, we present petrology, geochemistry, sphene U-Pb geochronology and trace element data from the syenogranite, quartz syenite and quartz monzonite of the Guandimiao alkaline complex rocks to investigate their petrogenesis. Geochemical data suggest that these alkaline rocks show alkalic and peralkaline characters, and high Ga/Al ratios, SiO_2, light rare-earth element (LREE), Zr and Nb, and low MgO, CaO, Eu contents, corresponding to A-type granites. Sphene trace elements in syenogranite and quartz monzonite show obvious fractionation between LREE and heavy rare-earth element (HREE) and high Th/U ratios, indicating a magmatic origin. They yield U-Pb lower intercept ages of 128 ± 2.3 Ma and 127 ± 1.3 Ma, representing the crystallization ages of these alkaline rocks. The negative correlations between CaO, Fe_2O_3 (Total), MgO, P_2O_5, TiO_2, MnO and the pronounced depletion in Nb, Ta and Ti suggest that the alkaline rocks were formed by fractional crystallization. Additionally, the positive correlation between La/Hf and La, Th and Th/V, Ce/Yb and K_2O, and Tb/Yb and Yb suggest that the alkaline melts are generated by partial melting. Such high Rb/Nb, $(Th/Nb)_N$ and Nb/Th ratios indicate crustal contamination during the magma emplacement. We, therefore, propose the magma source of the alkaline rocks in the Guandimiao complex originated by partial melting of lithospheric mantle, which experienced fractional crystallization and crustal contamination processes during its emplacement. Such complex alkaline rocks were probably formed in an extensional back-arc setting induced by the retreat of the subducting Izanagi plate.

Keywords: alkaline rock; whole-rock geochemistry; sphene U-Pb geochronology; sphene trace element geochemistry; Guandimiao REE deposit

Citation: Xi, Z.-C.; Qiu, K.-F.; Zhi, C.-L.; Li, S.-S.; Shang, Z.; Huang, Y.-Q. Partial Melting of Lithospheric Mantle and Formation of the Early Cretaceous Alkaline Rocks in the Guandimiao REE Deposit, Luxi Terrane, Eastern China. *Minerals* **2022**, *12*, 670. https://doi.org/10.3390/min12060670

Academic Editor: Silvio Giuseppe Rotolo

Received: 31 March 2022
Accepted: 16 May 2022
Published: 26 May 2022

1. Introduction

The Yanshanian orogenesis, correlated with the subduction of the Izanagi plate, resulted in widespread magmatism and ore formation in the Luxi Terrane [1–3], and formed a series of alkaline intrusive rocks and rare-earth element (REE) deposits in eastern China. Such REE deposits comprise the Weishan, Longbaoshan and Guandimiao REE deposits, which are spatially hosted by NW- and NWW-oriented faults [1–5]. Previous studies on the Early Cretaceous alkaline rocks in the Luxi Terrane indicate that the petrogenesis of the alkaline rocks remains controversial [6–9]. Previous studies proposed that decreases in TiO_2, Al_2O_3, Fe_2O_3 (Total), MnO, MgO, CaO and P_2O_5 with an increasing SiO_2 of

the Weishan and Longbaoshan alkaline complex were caused by fractional crystallization [5,6,8]. The presence of inherited zircon grains (2639–2494 Ma) in the Weishan and Longbaoshan complex is evidence of crustal contamination [5,6,8]. Moreover, as the SiO_2 contents increase, the Longbaoshan alkaline complex shows lower $(^{87}Sr/^{86}Sr)_i$ ratios and higher εNd(t) values, suggesting that the alkaline complex might have assimilated some crustal materials [8]. Liu et al. [7] interprets the positive correlation between La/Sm ratios and La abundance of the pyroxene syenite as partial melting, and the La/Sm ratios remain unchanged, with the increasing La content of the hornblendite as fractional crystallization for the Guandimiao complex. The presence of inherited zircon grains (2553–2178 Ma) from the pyroxene syenite of the Guandimiao complex suggests crustal contamination during magma emplacement [7]. The Guandimiao complex is composed of pyroxenites, hornblendites, dioritic porphyries, pyroxene syenites, quartz syenites, syenogranites and quartz monzonites, representing a fractionation sequence [7,10]. Previous studies have investigated the petrogenesis of the hornblendites and pyroxene syenites and proposed a fractional crystallization and partial melting model, with crust material contamination [7]. The petrogenesis of the alkaline sequence, including quartz syenites, syenogranites and quartz monzonites, however, remains ambiguous.

In the present study, we report the whole-rock geochemistry, sphene U-Pb geochronology and sphene trace-element geochemistry of the alkaline rocks in the Guandimiao complex. We aim to investigate the emplacement timing and origin of the alkaline sequence and shed light on the petrogenesis of the alkaline rocks in the Luxi Terrane, eastern China.

2. Geological Setting

The North China Block (NCB) has undergone a series of geodynamic events since the Mesozoic, including the collision of the NCB and Yangtze plate and subduction of the Izanagi plate, and compression-to-extension tectonic regime transformation, resulting in the thinning of the lithosphere associated with widespread magmatism and ore formation [11–15] (Figure 1A,B). The Luxi Terrane intersects to the east with the Liaocheng–Lankao fault zone, to the west with the Yishu fault zone, to the south with the Fengpei fault and to the north with the Qihe–Guangrao fault, forming an approximate parallelogram [6] (Figure 1C). The exposed formations in the southwest of the Luxi Terrane include Cambrian–Ordovician limestones, dolomites and shales, Palaeogene sandstones, and Quaternary clastic sediments (Figure 1D). The Luxi Terrane of the NCB experienced compressional deformation caused by the subduction of Izanagi plate during the Middle–Late Jurassic (170–135 Ma), resulting in the development of the EW-oriented Yicheng fault and smaller NE- and NW-oriented faults [16]. The magmatic activity is frequent, including Neoarchean, Neoproterozoic and Mesozoic magmatic events [2,10,16–19], leading to the formation of Precambrian and minor Mesozoic intrusive rocks [2]. Among them, the Mesozoic Yanshanian magmatic activity is relatively extensive and formed various types of magmatic rocks, including quartz syenites, syenites, bistagites and quartz syenite porphyries. Major commodities in the Luxi Terrane include iron, gold and REEs [2,6,20–22].

The Guandimiao area is located in the southwest Luxi Terrane (Figure 1D). The exposed formations in the area include Cambrian limestones and shales, Ordovician dolomites and limestones, and Quaternary clastic sediments. The Mesozoic Yanshanian magmatic activity is intensive, intruding into Archean granodiorites [7], and formed a series of magmatic rocks, including pyroxenites, hornblendites, dioritic porphyries, pyroxene syenites, quartz syenites, syenogranites and quartz monzonites.

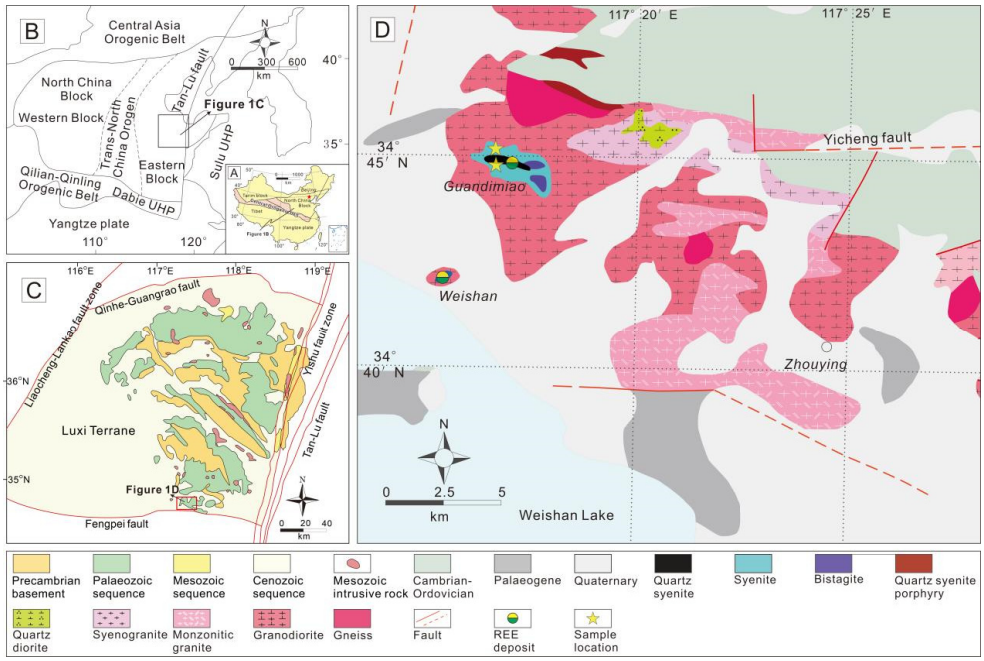

Figure 1. (**A**) Simplified geological sketch map of China [8]. (**B**) Simplified geological sketch map of the major tectonic units of eastern China [23,24]. (**C**) Geological sketch map of the Luxi Terrane. (**D**) Geological sketch map of the southwest Luxi Terrane.

3. Samples and Analytical Methods

The studied samples are collected from the Guandimiao REE deposit, and sample locations are marked in Figure 1D. Among them, the sample locations of the syenogranite (21XC01) and quartz syenites (21XC02, 21XC03, 21XC04, 21XC05) are 34°45′20″ N, 117°16′45″ E. The sample locations of the syenogranites (21XC07, 21XC08) and quartz monzonites (21XC06, 21XC09, 21XC10) are 34°44′54″ N, 117°16′50″ E. Ten samples, including three syenogranites, four quartz syenites and three quartz monzonites, were collected for geochemistry, and, among them, two samples (21XC01, 21XC06) were analyzed for sphene U-Pb dating.

3.1. Whole-Rock Geochemistry

Fresh samples were selected, crushed, and powdered to less than 200 mesh in an agate mill for whole-rock analysis. Geochemical data (major and trace elements) were obtained at the testing center of the Shandong Provincial Lunan Geology and Exploration Institute, China. Major elements were analyzed by X-ray fluorescence using a Rigaku RIX 2100 spectrometer with analytical uncertainties of 1–5%. Trace elements were determined using a PEE lan 6000 ICP-MS instrument with analytical uncertainties of 1–3%. Details of the analytical techniques are described in [25]. Analyses of basalt and andesite standard (BHVO-1, BCR-2, and AGV-1) indicated that the analytical precision and accuracy were better than 5% for major elements and 10% for trace elements and REEs [26].

3.2. Sphene LA-ICP-MS U-Pb Dating

The syenogranite and quartz monzonite samples were crushed to 40–60 mesh (250–380 μm) and sphene crystals were separated through standard magnetic and density separation techniques. Sphene grains were carefully handpicked under a binocular microscope, mounted in epoxy, polished down to near half-sections to expose internal structures, and then cleaned in an ultrasonic washer containing a 5% HNO_3 bath. Prior to analysis, polished sections of sphene were carbon coated for Back-Scattered-Electron (BSE, Langfang Regional Geological Survey, Hebei, China) analyses using a JXA-880 electron microscope. Image analysis software was used under operating conditions of 20 kV and

20 nA, at the Langfang Regional Geological Survey, Hebei Province, China, to identify the internal structure and texture of all sphene crystals. Sphene samples were checked carefully using the microscope and BSE images for fluid inclusions and cracks. LA-ICP-MS analyses were conducted at the Isotopic Laboratory, Tianjin Center, China Geological Survey. Details of the analytical procedures are given in [27,28].

Laser sampling was performed using a Neptune double-focusing multiple-collector ICP-MS attached to a NEW WAVE 193 nm-FX ArF Excimer laser-ablation system. All analyses were conducted with a beam diameter of 35 μm, an 8 Hz repetition rate, and energy density of 11 J/cm^2. GJ-1 was used as an internal standard for U-Pb dating analyses. NIST SRM 610 glass was used as an external standard to calculate U, Th, and Pb concentrations of sphene crystals. Every eight analyses were followed by two analyses of the standard zircon GJ-1. Isotopic ratios were calculated using ICPMSDataCal 8.4, China University of Geosciences, Wuhan, China [29] and were plotted using Isoplot version 3.0 software [30]. Common-Pb corrections were made following the methodology of [31].

4. Results

4.1. Petrography

The quartz syenites (21XC03, 21XC05) show light gray color, granular texture and massive structure (Figure 2A,B). The paragenesis of the quartz syenites are dominated by orthoclase (~60–61%), plagioclase (~24%), quartz (~6–9%), hornblende (~6–9%) and biotite (~1%) (Figure 3A–D). Accessory minerals include zircon, apatite and sphene. Orthoclase is subhedral to anhedral with crystal size of 180–3000 μm and typically show carlsbad twinning. Plagioclase is subhedral with crystal size of 200–2500 μm, shows polysynthetic twinning, and is partly altered sericite.

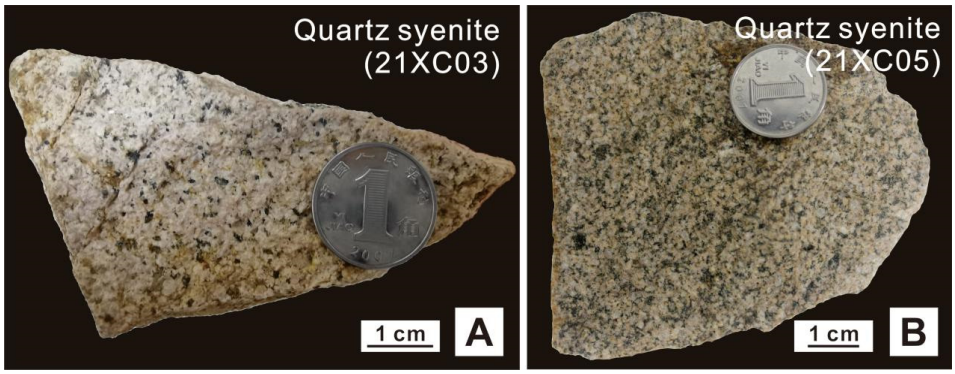

Figure 2. Hand specimen photographs of the alkaline rocks. (**A**) Quartz syenite (21XC03); (**B**) Quartz syenite (21XC05).

4.2. Geochemistry

Syenogranite, quartz syenite and quartz monzonite show high SiO_2 (61.6–74.9 wt.%), Al_2O_3 (11.8–14.3 wt.%), Na_2O (5.26–6.60 wt.%) and Zr (251–441 ppm) concentrations, and low CaO (0.97–2.41 wt.%), MgO (0.33–1.90 wt.%), TiO_2 (0.16–0.3 wt.%) and P_2O_5 (0.04–0.31 wt.%) content (Table 1). These rocks show a high R1 (4Si-11(Na+K)–2(Fe+Ti)) (934–2271) and R2 (6Ca+2Mg+Al) (374–496) ratios and correspond to quartz syenite and syenogranite compositions (Figure 4A). The studied samples, plotted in the alkalic and peralkaline fields, indicating that the complex is alkaline (Figure 4B,C). In terms of the alumina saturation index, the studied rocks are peralkaline ((Na+K)/Al>1; A/CNK: 0.75–0.88) (Figure 4D). Chondrite-normalized REE patterns of three syenogranites, four quartz syenites and three quartz monzonites show pronounced LREE enrichment, HREE depletion and slightly positive Eu anomalies (Eu/Eu*: 1.00–1.14) with high ratios for $(Gd/Yb)_N$: 6.1–12.6, $(La/Yb)_N$: 59.6–131.9 and $(La/Sm)_N$: 4.6–6.1 (Figure 5A). Primitive mantle-normalized trace element patterns show enrichment in large ion lithophile elements (LILEs) Rb and Ba, and depletion in high-field-strength elements (HFSEs) Nb, Ta, Ti (Figure 5B).

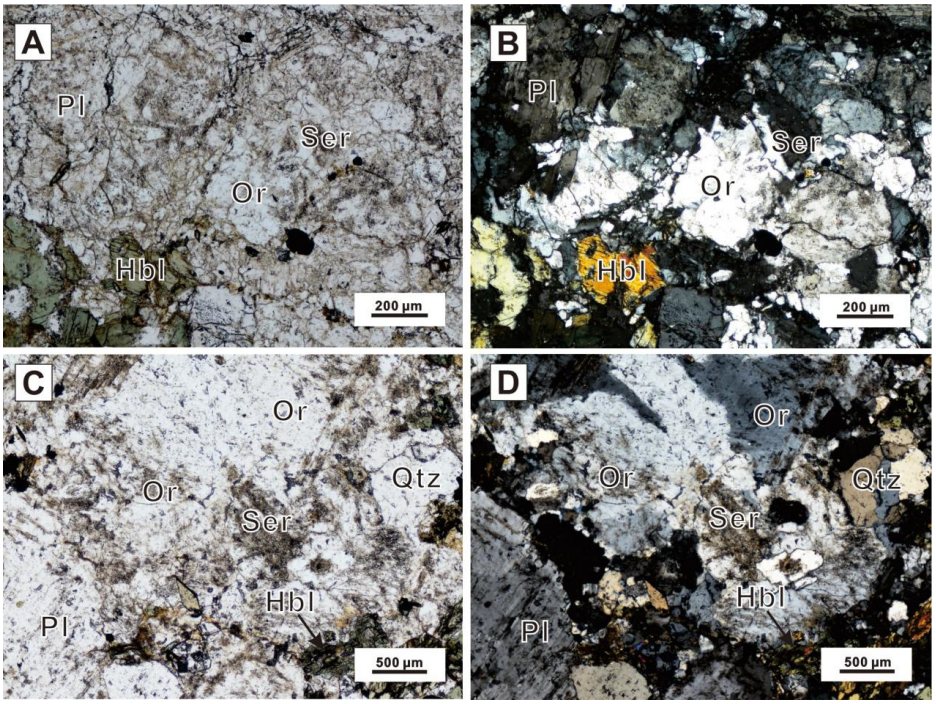

Figure 3. Optical microscopy photomicrographs of the alkaline rocks. (**A**,**B**) Quartz syenite (21XC03); (**C**,**D**) Quartz syenite (21XC05). Mineral abbreviations: Pl—plagioclase; Or—orthoclase; Hbl—hornblende; Qtz—quartz; Srt—sericite. (**A**,**C**) plane-polarized light, (**B**,**D**) cross-polarized light.

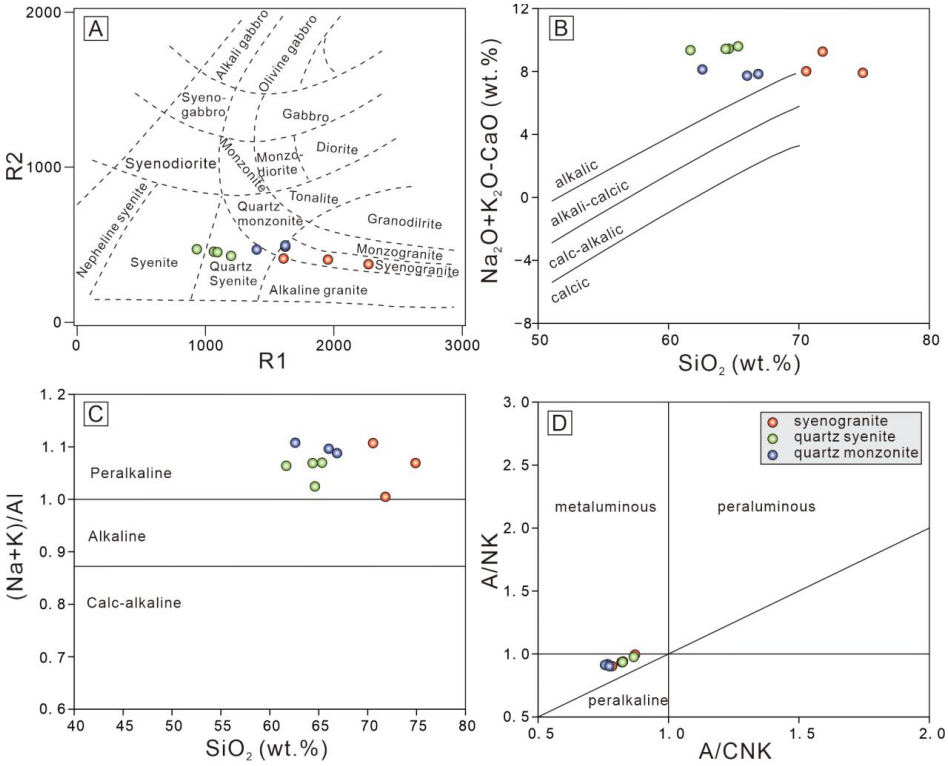

Figure 4. Geochemical classification plots of the syenogranite, quartz syenite and quartz monzonite. (**A**) R2 (6Ca + 2Mg + Al) vs. R1 (4Si—11(Na + K)—2(Fe + Ti)) plot for classifying the rock types [32]. (**B**) (Na_2O + K_2O—CaO) vs. SiO_2 [33] classification diagram for evaluating the calcic to alkalic variations. (**C**) (Na + K)/Al vs. SiO_2 plot [34]. (**D**) A/NK [molar $Al_2O_3/(Na_2O + K_2O)$] vs. A/CNK [molar $Al_2O_3/(CaO + Na_2O + K_2O)$] for evaluating peralkaline, metaluminous and peraluminous melt compositions [35].

Table 1. Major and trace element compositions for the alkaline rocks.

Sample	21XC01	21XC02	21XC03	21XC04	21XC05	21XC06	21XC07	21XC08	21XC09	21XC10
	Syeno-granite	Quartz Syenite	Quartz Syenite	Quartz Syenite	Quartz Syenite	Quartz Monzonite	Syeno-granite	Syeno-granite	Quartz Monzonite	Quartz Monzonite
Major elements (wt.%)										
SiO_2	71.8	64.6	65.3	61.7	64.4	66.9	74.9	70.6	66	62.6
Al_2O_3	14.3	14.2	14.3	14.1	14	12.4	11.8	11.8	12.1	12.2
TiO_2	0.3	0.3	0.2	0.2	0.2	0.2	0.2	0.2	0.2	0.2
Fe_2O_3	3	2.6	1.7	1.9	1.8	1.6	1.5	1.3	1.5	1.5
FeO	0.2	0.2	0.5	0.4	0.5	0.6	0.2	0.2	0.6	0.4
CaO	1.1	1	1.1	1.1	1.1	1.5	1	1.1	1.5	1.2
MgO	0.4	0.3	0.6	0.6	0.5	1.1	0.7	0.7	1.2	0.9
K_2O	4.8	4.7	4.1	4.1	4.2	3.3	3.6	3.4	3.4	3.5
Na_2O	5.6	5.7	6.6	6.4	6.3	6	5.3	5.7	5.8	5.9
MnO	0.1	0.1	0	0.1	0	0	0	0	0	0
P_2O_5	0.3	0.3	0.1	0.1	0.1	0.2	0.1	0.1	0.2	0.1
LOI	1.8	1.8	0.7	0.3	0.7	0.7	1	0.7	0.5	0.5
A/CNK	0.9	0.9	0.8	0.8	0.8	0.8	0.8	0.8	0.8	0.8
A/NK	1	1	0.9	0.9	0.9	0.9	0.9	0.9	0.9	0.9
Trace elements (ppm)										
La	162.3	153.1	80.6	84.2	86.5	81.4	61.8	70.3	66.5	73.5
Ce	347	335.9	183.8	192.8	192.4	184.5	135	148.1	156.1	153.7
Pr	42.8	38.7	21.7	22.9	23.3	21.1	14.9	15.9	18.2	16.7
Nd	163.2	145.7	84	88	90.1	79.7	56.2	58.6	70.4	61.8
Sm	19.9	18.6	11	11.3	11.6	10.5	7.2	7.5	9.3	7.9
Eu	5.6	5.1	3.2	3.3	3.4	3	2.1	2.2	2.7	2.2
Tb	1.4	1.1	0.8	0.8	0.9	0.7	0.5	0.5	0.8	0.6
Dy	5.8	4.9	3.5	3.7	3.9	3.6	2.8	2.6	3.6	2.8
Ho	0.7	0.6	0.4	0.4	0.5	0.4	0.3	0.3	0.5	0.4
Er	1.9	1.5	1.1	1.3	1.2	1.2	1	0.9	1.3	1
Cu	17	22.5	4.8	6.2	5.6	8.2	6.5	5.2	5.6	4.1
V	76.5	66.8	46.7	48.8	46.6	38.9	27.7	24.3	35.6	30.9
Ba	4858	4870.5	3067.4	2957.8	3160.8	3733.9	2875.8	2846.2	3532.3	3172.3
Gd	12.5	12.7	6.9	7.5	7.5	6.7	4.8	5	6.2	5.3
Ni	21.1	19.3	19.3	21.6	20.2	35.9	25.7	22.7	36	26
Zn	32.5	43.3	33.9	35.4	32.9	35.1	23.3	24.1	39.9	41.9
Cr	27.8	13.2	14.4	17.6	27.4	22.3	24.8	9.4	23.7	14.7
Pb	32.4	39.5	30.1	32.2	32.6	32.6	28.6	31.8	32.4	32.1
Sc	4.2	2.4	3	3.1	2.3	2.4	2	1.8	2.5	1.6
Ga	36.8	34.9	28.7	29.4	29.6	27.9	25.6	25.8	27.7	27.8
Rb	61.3	58.7	64	64.6	66.4	59	65.3	63.9	62	63.5
Sr	3206.2	3051.9	2152.6	2075.4	2205.8	2237.6	1629.3	1775.5	2115.5	2024.6
Y	21.4	18.5	13.3	14.1	14.8	13.4	11.3	11.5	15.1	11.7
Zr	410.6	441.4	401.7	381.9	413.6	333.5	250.7	290	348.1	292.8
Nb	30.6	20.2	7.5	7.1	8.4	15.4	15.1	12.6	16.2	16.5
Cs	0.5	0.5	0.7	0.7	0.8	0.5	0.4	0.6	0.5	0.6
Tm	0.2	0.1	0.1	0.1	0.1	0.1	0.1	0.1	0.1	0.1
Yb	1	0.8	0.7	0.7	0.7	0.7	0.7	0.7	0.8	0.6
Lu	0.1	0.1	0.1	0.1	0.1	0.1	0.1	0	0.1	0
Hf	2.6	2.3	1.8	1.9	1.6	2.2	2.8	2.3	2.2	2.2
Ta	0.8	0.4	0.3	0.3	0.5	0.5	0.7	0.4	0.5	0.8
Th	6.2	7.1	6.2	7.7	7.1	6.6	13.4	16.8	8.2	12.6
U	2	1.7	0.9	1	0.9	2	2.5	2.2	1.9	1.9

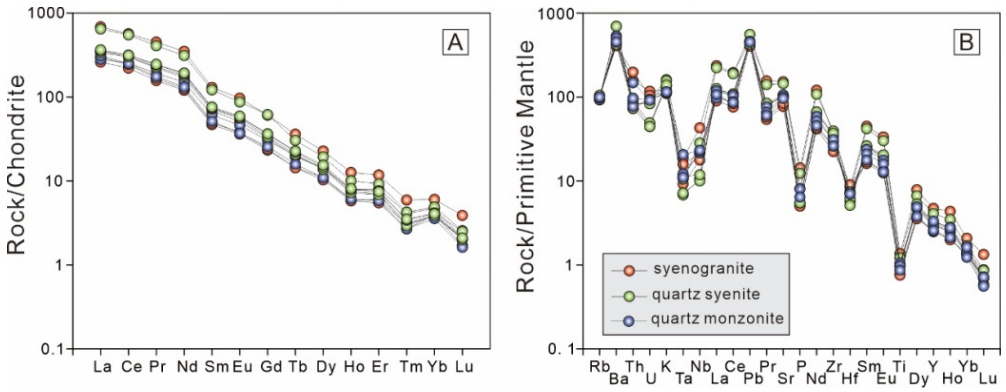

Figure 5. (**A**) Chondrite-normalized REE patterns [36]; (**B**) Primitive mantle-normalized trace element patterns [37].

4.3. Sphene U-Pb Geochronology

Two samples were dated for sphene U-Pb geochronology, syenogranite and quartz monzonite, with LA-ICP-MS data given in Table 2, the morphology shown in Figure 6 and data plotted in Figure 7.

Table 2. LA-ICP-MS sphene U-Pb isotope data of syenogranite and quartz monzonite.

Sample	Th (ppm)	U (ppm)	Th/U	$^{207}Pb/^{206}Pb$	1σ	$^{207}Pb/^{235}U$	1σ	$^{206}Pb/^{238}U$	1σ
21XC01									
21XC01-1	490	110	4.458	0.5474	0.0054	3.8327	0.0465	0.0508	0.0005
21XC01-2	276	31.3	8.818	0.653	0.0071	6.5404	0.0878	0.0728	0.0008
21XC01-4	379	56.9	6.655	0.5389	0.0128	3.5384	0.0701	0.0481	0.0007
21XC01-5	310	36.1	8.592	0.6408	0.0168	5.8779	0.1738	0.0672	0.0018
21XC01-6	396	48.2	8.204	0.5184	0.0179	3.0258	0.0694	0.0437	0.001
21XC01-7	249	28.9	8.612	0.7	0.0092	7.8703	0.1594	0.0815	0.0012
21XC01-8	354	38.4	9.229	0.5645	0.0068	4.1937	0.0397	0.0543	0.0006
21XC01-9	163	23.5	6.942	0.6382	0.0084	5.9099	0.083	0.0677	0.0009
21XC01-10	323	40.6	7.965	0.5791	0.0148	3.914	0.0731	0.0499	0.0008
21XC01-11	266	26	10.198	0.6887	0.0088	8.6569	0.0971	0.0918	0.0013
21XC01-12	233	26.2	8.88	0.7107	0.0104	9.1349	0.22	0.0934	0.0019
21XC01-13	286	29.5	9.687	0.7001	0.0154	9.7558	0.3149	0.1014	0.0026
21XC01-14	505	99.6	5.07	0.6444	0.0085	7.0309	0.2272	0.0778	0.0019
21XC01-15	214	26	8.211	0.674	0.0072	7.9791	0.0653	0.0864	0.0008
21XC01-16	374	49.4	7.569	0.5417	0.0123	3.6744	0.1201	0.049	0.0009
21XC01-17	215	23.8	9.002	0.699	0.0076	9.7453	0.275	0.1005	0.0023
21XC01-19	246	29.4	8.36	0.7156	0.0069	10.1423	0.1824	0.1028	0.0016
21XC01-20	270	30.4	8.88	0.6592	0.009	6.8915	0.0669	0.0766	0.0009
21XC01-21	312	57.5	5.433	0.4722	0.0132	2.7544	0.0525	0.0429	0.0009
21XC01-22	436	48.7	8.954	0.5245	0.0078	3.5234	0.041	0.0492	0.0006
21XC01-23	279	27.2	10.253	0.6569	0.0089	7.1896	0.1222	0.0796	0.0011
21XC01-24	292	42.5	6.858	0.5872	0.0073	4.8237	0.0814	0.0596	0.0008
21XC01-25	175	21.6	8.124	0.6798	0.0082	7.2739	0.0857	0.0783	0.0009
21XC01-26	251	29.4	8.519	0.5833	0.0068	4.6088	0.069	0.0575	0.0007
21XC01-27	378	46.5	8.129	0.5376	0.0083	3.6907	0.0453	0.0502	0.0006
21XC01-28	288	32.2	8.941	0.6211	0.008	5.248	0.0609	0.0617	0.0006
21XC01-29	320	45.9	6.966	0.5369	0.0107	3.4069	0.0541	0.0466	0.0006
21XC01-30	222	27.1	8.219	0.6808	0.038	7.3863	0.3609	0.081	0.0043
21XC06									
21XC06-1	444	72.7	6.105	0.5199	0.0065	3.2869	0.0377	0.046	0.0005
21XC06-2	376	68.7	5.473	0.5628	0.0104	3.8959	0.0661	0.0504	0.0008
21XC06-4	244	138	1.773	0.3285	0.0049	1.3758	0.0248	0.0304	0.0003
21XC06-5	289	158	1.831	0.3008	0.0043	1.2044	0.0154	0.0292	0.0002
21XC06-7	316	109	2.894	0.4015	0.0095	1.9311	0.0632	0.0347	0.0006
21XC06-8	329	176	1.871	0.2882	0.0055	1.1087	0.0245	0.0279	0.0003
21XC06-9	340	118	2.87	0.3671	0.0063	1.5963	0.0242	0.0317	0.0004
21XC06-10	369	298	1.238	0.1926	0.002	0.6517	0.0076	0.0245	0.0002
21XC06-11	273	59.5	4.593	0.6038	0.0144	4.602	0.1677	0.0548	0.0014
21XC06-12	433	63.5	6.818	0.5707	0.0053	4.2066	0.0323	0.0537	0.0004
21XC06-13	321	55.5	5.786	0.5693	0.0075	4.1252	0.0509	0.0529	0.0007
21XC06-14	462	208	2.222	0.2565	0.0033	0.9149	0.0111	0.0259	0.0002
21XC06-15	348	268	1.298	0.2165	0.003	0.7424	0.0108	0.0248	0.0002
21XC06-16	276	188	1.468	0.3431	0.0044	1.4844	0.0146	0.0314	0.0003
21XC06-17	342	53.1	6.437	0.5874	0.0053	4.3403	0.0406	0.0537	0.0005
21XC06-19	343	63.7	5.374	0.5384	0.0064	3.5975	0.0633	0.0484	0.0006
21XC06-20	417	68.7	6.073	0.5952	0.0066	4.6097	0.0565	0.0564	0.0005
21XC06-21	430	124	3.47	0.3607	0.0042	1.5262	0.0163	0.0308	0.0002
21XC06-22	359	281	1.279	0.2017	0.0029	0.6553	0.0103	0.0236	0.0002
21XC06-23	319	59.4	5.372	0.6424	0.006	6.0834	0.0555	0.0691	0.0007
21XC06-24	428	155	2.759	0.2782	0.0041	1.0734	0.0136	0.0282	0.0002
21XC06-26	354	233	1.519	0.2469	0.0033	0.9143	0.0156	0.0267	0.0002
21XC06-27	291	132	2.198	0.2526	0.0041	0.8642	0.0139	0.0249	0.0002
21XC06-28	426	201	2.115	0.4463	0.0214	2.5961	0.1374	0.0422	0.0008
21XC06-29	397	79	5.022	0.5916	0.006	4.3879	0.0806	0.0538	0.0008
21XC06-30	360	192	1.876	0.2308	0.0041	0.8092	0.0151	0.0256	0.0004
21XC06-31	264	48.8	5.414	0.6179	0.0081	5.2403	0.0485	0.0619	0.0007
21XC06-32	283	90.9	3.107	0.4628	0.007	2.3847	0.0394	0.0375	0.0004

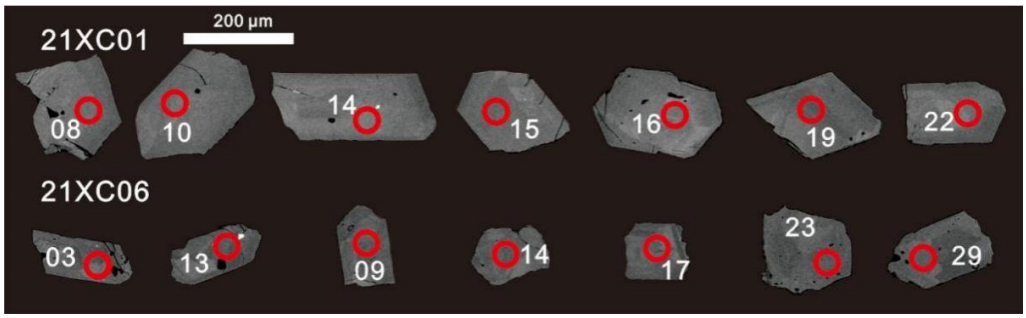

Figure 6. BSE image of sphene grains from syenogranite and quartz monzonite. The red circles indicate spots of LA-ICP-MS U-Pb dating.

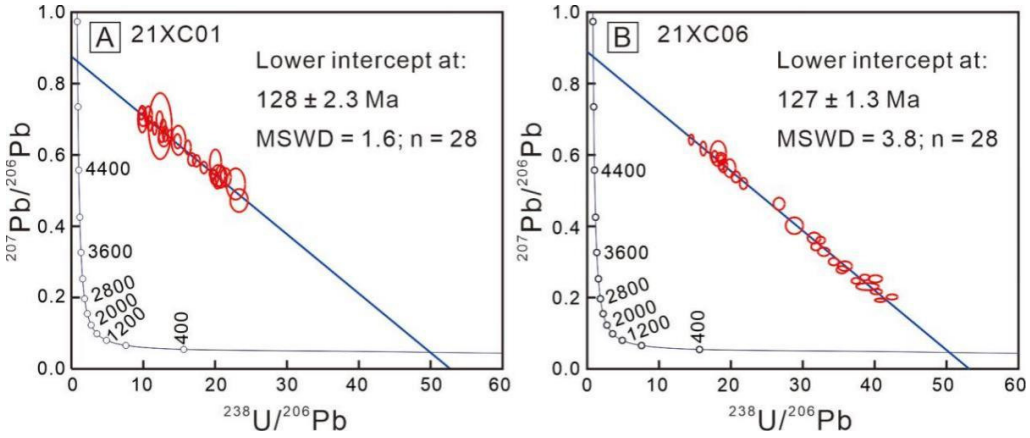

Figure 7. Sphene U-Pb lower intercept ages plots: (**A**) for syenogranite; (**B**) for quartz monzonite.

Sphene grains from syenogranite (21XC01) are euhedral–subhedral and range from 180 to 300 μm in size, with length-to-width ratios of from 1:1 to 2:1 (Figure 6). Twenty-eight spots were analyzed on 28 grains. The 28 analyses yield lower intercept dates of 128 ± 2.3 Ma (2σ, *n* = 28, MSWD = 1.6) (Figure 7A). The Th contents range from 163 to 505 ppm and U contents range from 22 to 110 ppm. They show Th/U ratios of 4.4 to 10.3 (Table 2).

Sphene grains in quartz monzonite (21XC06) are subhedral in shape, with a length of 100–200 μm and aspect ratio of 1:1 to 2:1 (Figure 6). Twenty-eight spots were analyzed on 28 grains. The analyzed spots yield lower intercept dates of 127 ± 1.3 Ma on a Tera–Wasserburg diagram (2σ, *n* = 28, MSWD = 3.8) (Figure 7B). They show Th and U contents of from 244 to 462 ppm and 48 to 298 ppm. The Th/U ratios range from 1.2 to 6.9 (Table 2).

4.4. Trace Element Geochemistry of Sphene

Sphene REE data from the syenogranite (21XC01) shows the high total REE, respectively ranging from 26,594 to 44,233 ppm and 25,538 to 42,146 ppm, and low HREE content of 953 to 2267 ppm (Table 3). All REE data from syenogranite exhibit similar chondrite-normalized REE patterns with pronounced LREE enrichment and HREE depletion, strong fractionation from LREE to HREE ($(La/Yb)_N$ = 26–81) and HREE ($(Gd/Yb)_N$ = 4–13), with slightly negative Eu anomalies (Eu/Eu* = 0.66–1.06) (Figure 8A).

Table 3. Trace-element compositions for the sphene in the alkaline rocks (ppm).

Spot	La	Ce	Pr	Nd	Sm	Eu	Gd	Tb	Dy	Ho	Er	Tm	Yb	Lu	Ce/Ce *	Eu/Eu *
21XC01-1	7226	19231	2309	8539	1335	249	817	98.6	468	77.9	176	22	120	12.8	1.1545	0.7305
21XC01-2	6710	16779	1917	6814	879	221	484	53	244	40.1	92.9	11.7	66	7.2	1.147	1.0345
21XC01-3	5552	15338	1976	7924	1348	295	776	88.3	391	58.6	128	14.2	77.1	8.01	1.1353	0.8809
21XC01-4	5483	15328	1927	7603	1267	272	770	89	407	65.5	144	17.6	97.7	10.3	1.1559	0.8408
21XC01-5	5718	16347	2139	8697	1439	264	846	91.7	421	64.6	141	17.3	96.4	10.6	1.146	0.7319
21XC01-6	5506	12538	1389	5282	829	209	477	51.2	229	36	79.1	9.93	62.8	7.96	1.1116	1.0133
21XC01-7	6303	18347	2437	10047	1636	334	951	104	450	68.4	144	16.5	87.6	9.02	1.1478	0.8193
21XC01-8	5554	15099	1866	7307	1182	254	719	81.4	370	59.2	133	16.3	93	10.4	1.1499	0.843
21XC01-9	5281	15525	2117	8950	1429	304	792	83.4	352	51.9	105	11.7	60.4	6.16	1.1384	0.8734
21XC01-10	4991	12953	1513	5543	845	201	514	59.2	280	46.3	111	14.1	85.6	9.8	1.1557	0.931
21XC01-11	5157	16467	2367	10455	1898	339	1127	122	532	79.2	162	18	93.6	9.72	1.1556	0.7093
21XC01-12	6425	19036	2556	10626	1746	320	1003	109	473	71.3	148	17.1	89.3	9.33	1.1517	0.7384
21XC01-13	6077	17634	2332	9491	1568	302	921	104	469	72.4	155	18.2	96.8	10.1	1.1484	0.7686
21XC01-14	4847	13329	1730	7120	1216	326	737	87	408	66.8	152	19.1	109	12.3	1.1288	1.0526
21XC01-15	6833	17002	1987	7234	997	229	555	60.1	273	42.5	93.4	11.2	60.7	6.27	1.1315	0.9396
21XC01-16	6664	19831	2659	10863	1793	336	1057	117	528	80.2	170	19.7	104	10.7	1.155	0.7469
21XC01-17	4961	15042	2058	8705	1482	276	858	93.9	411	61.7	130	14.9	79.6	8.37	1.1544	0.7487
21XC01-18	5352	14411	1826	7154	1178	248	681	78.5	359	55.7	127	15.5	81.6	8.88	1.1302	0.8452
21XC01-19	5390	14466	1746	6610	1017	221	594	67.2	306	48.8	110	13.6	75.4	8.07	1.1561	0.871
21XC01-20	5652	15278	1830	6770	1016	216	584	66.4	310	50.4	114	14.2	79.3	8.66	1.1647	0.8584
21XC01-21	5000	12613	1480	5393	836	217	492	55.9	262	42.8	103	13.1	78.4	9.32	1.137	1.0326
21XC01-22	5870	14788	1661	6058	910	210	544	62.1	293	48.2	115	14.7	89.5	10.2	1.1613	0.9108
21XC01-23	5617	17803	2548	11082	1977	332	1172	130	562	84.9	178	20.3	108	11.2	1.1537	0.6661
21XC01-24	5976	17105	2231	8987	1475	292	856	96.4	430	67.3	146	17.2	92	9.58	1.1484	0.7958
21XC01-25	5839	17293	2415	10325	1720	369	961	100	419	60.1	118	12.8	64.5	6.48	1.1291	0.8779
21XC01-26	6023	17293	2333	9840	1643	364	923	96.3	404	58	114	12.6	65.9	6.92	1.1311	0.9035
21XC01-27	5708	13959	1627	6106	950	226	552	60.8	273	43	97.9	12.6	74.4	8.96	1.123	0.9555
21XC01-28	5998	15614	1869	6929	1012	230	580	64.1	291	47	107	13.2	76.3	8.4	1.1434	0.9187
21XC01-29	4581	14144	1970	8364	1557	297	942	109	496	78	174	21.6	122	13.1	1.1544	0.7505
21XC01-30	5104	14904	1943	7781	1312	269	763	85.6	397	60.7	133	15.5	81.6	8.67	1.1603	0.8229
21XC06-1	4572	15079	2177	8920	1721	252	1124	144	689	111	240	28.4	150	14.9	1.1718	0.5532
21XC06-2	4182	13729	1978	8747	1701	270	1035	123	552	85.5	183	21.7	121	12.3	1.1703	0.6226
21XC06-3	3517	11756	1817	8326	1751	311	1107	134	614	93	188	21.9	116	11.7	1.14	0.6823
21XC06-4	4446	13021	1739	7105	1113	332	615	65	288	46	106	14.1	83.9	9.27	1.1482	1.2252
21XC06-5	4650	13434	1784	7286	1152	353	631	66.2	286	45	103	13.4	82.9	9.72	1.1436	1.2664
21XC06-6	4328	14028	1997	8407	1454	243	831	94.2	428	72	171	24.1	153	18.5	1.1699	0.6748
21XC06-7	4574	14518	2046	8765	1618	318	1001	117	532	81.4	177	21.2	117	12.1	1.1635	0.7634
21XC06-8	4641	13829	1817	7230	1087	245	588	63.2	280	45.6	107	14.7	92.1	11.2	1.1676	0.9354
21XC06-9	4142	13580	1980	8347	1407	328	803	86.8	390	62.2	140	17.9	102	11	1.1626	0.9432
21XC06-10	4779	15036	2077	8605	1472	273	841	95	431	70.1	163	22.2	136	15.6	1.1701	0.7508
21XC06-11	3641	12963	2119	10081	2398	412	1604	194	863	125	247	28.1	141	14	1.1444	0.6417
21XC06-12	3844	14041	2326	11461	2933	362	2071	259	1142	165	322	35.1	172	16.5	1.1515	0.449
21XC06-13	3906	13134	1941	8414	1757	254	1166	146	680	106	221	25.9	132	13	1.1697	0.5418
21XC06-14	6280	17110	2190	8571	1229	377	644	65.4	277	43.2	97.7	12.7	79	9.17	1.1313	1.2936
21XC06-15	5405	15787	2152	8875	1461	478	812	87.2	376	59.4	137	18.1	111	12.8	1.1349	1.3414
21XC06-16	4221	12204	1593	6256	964	239	537	58	257	40.2	89.6	11.6	70.8	8.29	1.1538	1.0144
21XC06-17	4158	14543	2280	10470	2297	362	1506	184	827	124	255	28.7	146	14.4	1.158	0.5951
21XC06-18	3909	12653	1834	7869	1387	242	807	91.3	416	69.3	166	22.7	142	17	1.1586	0.7004
21XC06-19	3980	13627	2127	9694	2194	334	1488	185	836	126	259	29.1	150	14.5	1.1483	0.5649
21XC06-20	4306	14194	1978	8016	1176	205	631	67.1	302	50.5	119	15.9	97.2	10.7	1.1924	0.7275
21XC06-21	4793	14369	2116	9572	1752	425	993	103	415	57.3	109	11.8	60.9	6.32	1.1064	0.9858
21XC06-22	4585	13468	1705	6363	926	231	502	55.2	257	43.7	111	16.4	115	14.7	1.1812	1.0331
21XC06-23	5146	15416	2019	7856	1115	197	591	61.7	273	43.4	98.3	12.9	77.2	8.4	1.1725	0.7433
21XC06-24	6910	17367	2010	7235	876	264	420	40	169	27.6	65.9	8.74	51.9	5.54	1.1426	1.3313
21XC06-25	3850	12273	1692	6866	1070	279	574	59	259	41.2	94.7	12.8	78.8	9.24	1.179	1.0871
21XC06-26	4895	15051	2080	8631	1414	351	778	81.9	357	57.1	132	17.7	111	13.6	1.1564	1.0245
21XC06-27	5245	15716	2159	9049	1496	452	826	85.6	356	53.4	113	13.9	77.9	8.11	1.145	1.243
21XC06-28	3967	13490	2022	9087	1971	350	1241	153	706	109	221	26.5	152	17.8	1.1677	0.6846
21XC06-29	4729	15137	2025	7943	1131	199	606	63.7	283	46.6	106	14	84	9.07	1.1993	0.7331
21XC06-30	5416	15285	1977	7873	1210	338	646	65	271	41.4	90.5	11.6	71.6	8.49	1.1452	1.1673
21XC06-31	2969	11130	1865	9218	2460	404	1735	218	962	142	281	30.1	148	14.1	1.1595	0.5978
21XC06-32	4099	14231	2165	9788	2101	362	1342	157	697	103	209	24.1	129	13	1.1713	0.6593

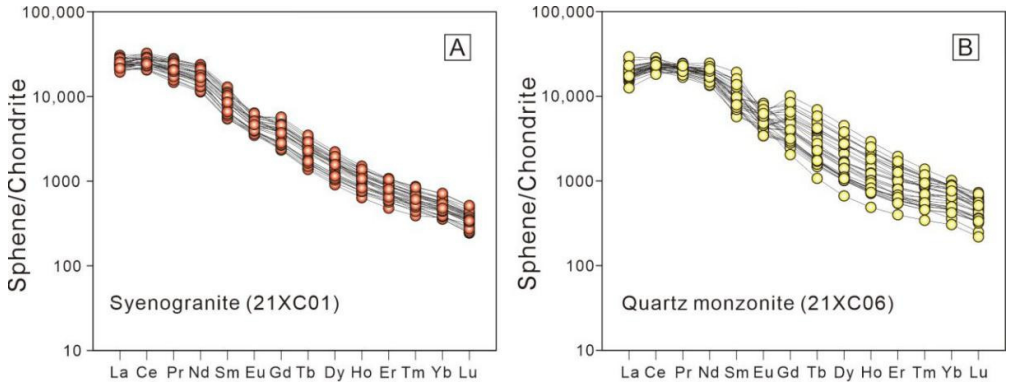

Figure 8. Chondrite-normalized REE patterns plots: (**A**) for sphene in syenogranite (21XC01); (**B**) for sphene in quartz monzonite (21XC06).

Total REE content of sphene from the quartz monzonite (21XC06) ranges from 26,550 ppm to 39,149 ppm. The LREE and HREE contents range from 25,477 ppm to 35,757 ppm, 788 ppm to 4182 ppm, respectively (Table 3). Chondrite-normalized REE patterns of the sphene in quartz monzonite show pronounced LREE enrichment, HREE depletion, strong fractionation of LREE/HREE ($(La/Yb)_N$ = 14–96) and discrete Eu anomalies (Eu/Eu* = 0.44–1.35) (Figure 8B). The HREE exhibit strong fractionation ($(Gd/Yb)_N$ = 3–14) with variable enrichment comparable to the syenogranite.

5. Discussion

5.1. Early Cretaceous Alkaline Magmatism in the Luxi Terrane

Sphene grains from syenogranite (21XC01) and quartz monzonite (21XC06) are euhedral–subhedral, with lengths of 100–300 μm (Figure 6), and the chondrite-normalized REE patterns show pronounced LREE enrichment, and HREE depletion, implying a magmatic origin (Figure 8) [38–41]. The Th/U ratios of the sphenes from the syenogranite and quartz monzonite are relatively high (>1) [39–42], supporting the magmatic origin. The sphene trace element data mostly fall in the magmatic field (Figure 9), which further implies a magmatic origin. Therefore, the lower intercept age of 127–128 Ma from the sphenes in syenogranite and quartz monzoite represent the crystallization age [43]. Liu et al. [7] reported LA-ICP-MS zircon U-Pb age of 128 Ma from pyroxene syenite in Guandimiao alkaline complex, which is consistent with the calculated sphene ages in this study. Therefore, the crystallization ages of alkaline rocks in the Guandimiao complex are bracketed in the range of 127–128 Ma.

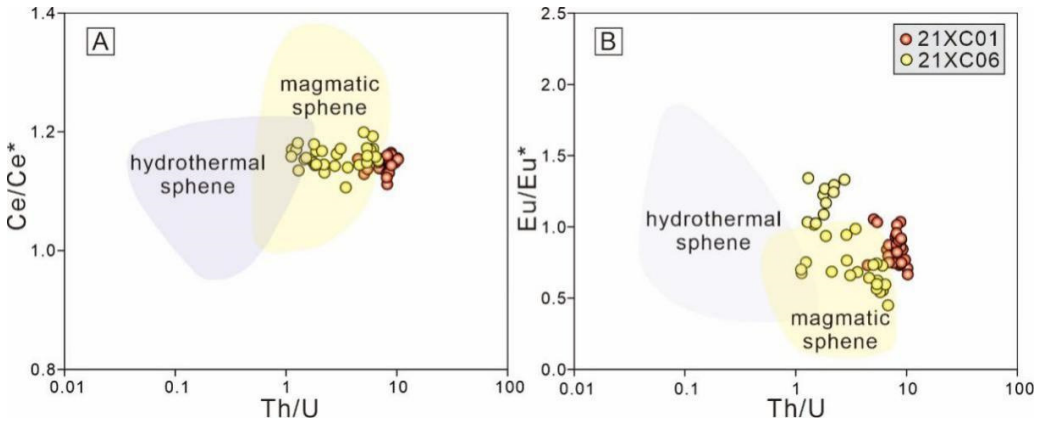

Figure 9. Sphene origin discrimination diagrams. (**A**) Ce/Ce* vs. Th/U [42] and (**B**) Eu/Eu* vs. Th/U [42] for the sphene from syenogranite and quartz monzonite.

Liang et al. [6] reported zircon U-Pb ages of 122–130 Ma for the quartz syenite and aegirine-augite syenite from the Weishan complex. Zircon grains from the quartz syenite and alkaline granites of the Weishan complex were dated by LA-ICP-MS at 125–127 Ma [9], and crystallization ages of 129–131 Ma were given for the Longbaoshan alkaline rocks by Lan et al. [8]. Hence, the Early Cretaceous alkaline magmatism in the Luxi Terrane occurred from 122 to 131 Ma, and formed a series of alkaline rocks.

5.2. Petrogenesis and Magma Origin

The Guandimiao complex consists of pyroxenites, hornblendites, dioritic porphyries (128 Ma), pyroxene syenites (128 Ma), quartz syenites, syenogranites (128 Ma) and quartz monzonites (127 Ma) with different compositions varying from ultramafic to acidic rocks [7,10], which may suggest the fractional crystallization model. To address the fractional crystallization process, we discussed the previously published hornblendite and the alkaline rocks in this study [7]. The negative correlations between major elements and SiO_2 suggest that the alkaline rocks are likely the result of fractional crystallization during magmatic evolution (Figure 10) [6,44]. The decreases in CaO, Fe_2O_3 (Total) and MgO with increasing of SiO_2 were probably caused by the fractional crystallization of hornblende and biotite (Figure 10A-C), which is consistent with the occurrence of hornblende and biotite in the Guandimiao complex. The negative correlation between SiO_2 and P_2O_5 implies the crystallization of apatite (Figure 10D), which is consistent with the occurrence of apatite. The differences in the HREE patterns indicate that the magma source is highly evolved, and silica and titanium are unsaturated in the quartz monzonite (Figure 8). The negative anomalies of the Nb, Ta and Ti are accounted for in the crystallization rutile and sphene (Figure 5B). The alkaline rocks contain abundant sphene and no rutile. Furthermore, the TiO_2 contents decrease with increases in SiO_2, implying that ilmenite and rutile may form as restite during the early fractional crystallization, while sphene formed during the later stage (Figure 10E). In summary, the major and trace-element geochemistry indicates that fractional crystallization played an important role in the formation of the alkaline rocks.

Since the La/Hf, Th/V, Ce/Yb and Tb/Yb ratios are sensitive to magmatic processes, they can be used to determine the different magmatic processes, including the partial melting and fractional crystallization [18,21,45]. On the La/Hf-La, Th-Th/V, Ce/Yb-K_2O and Tb/Yb-Yb discrimination diagrams (Figure 11), the alkaline rocks under examination exhibit a positive correlation between La/Hf and La, Th and Th/V, Ce/Yb and K_2O, and Tb/Yb and Yb, which are consistent with the partial melting trend, demonstrating the role of partial melting in generating the alkaline melts.

The alkaline rocks represent Rb/Nb ratios between 2.00 and 9.06 (average 5.07), which are close to the crust ratios (5.36–6.55) and significantly higher than the mantle ratios (0.24–0.89). Therefore, the Rb/Nb ratios of the alkaline rocks support crustal contamination to some degree. The alkaline rocks show $(Th/Nb)_N$ ratios 1.69 to 11.16, implying that the alkaline rocks have assimilated crustal material ($(Th/Nb)_N > 1$) [46]. In addition, the Nb/Th ratio is considered a critical indicator for crustal contamination processes [36]. The alkaline rocks with Nb/Th ratios between 0.75 and 4.95 are further consistent with those observed in the crust (~1.1), which substantiate the involvement of crustal material. The crustal contamination is further supported by the presence of inherited zircon grains (2553–2178 Ma) in the Guandimiao pyroxene syenite [7].

The Nb/Ta ratios (18.1–46.9) of the alkaline rocks are higher than the ratios of average crust (12–13) [47], which is consistent with the mantle source (15.5–19.5) [46], implying a mantle origin. Seven samples show Y/Nb ratios of lower than 1.2, which is also consistent with a mantle source (<1.2) [48–50], implying that the primary alkaline magma derived from the mantle. The La/Nb and La/Ta ratios (4.1–11.8, and 87–355 respectively) are close to the lithospheric mantle (La/Nb>1), and significantly higher than the ratios of the asthenosperic mantle (La/Nb = ~0.7, and La/Ta = ~10 respectively), implying lithospheric mantle origin [51,52]. These alkaline rocks fall within or near the enriched mantle field (Figure 12), which further implies the lithospheric mantle origin [53]. Three samples of

the alkaline rocks with Y/Nb ratios higher than 1.2 are consistent with a crustal source (>1.2) [49,50], which may be the result of crustal assimilation during magma emplacement. Zircon grains in the Weishan alkaline rocks display negative εHf(t) values ranging from −22.67 to −13.19 and yield a T_{DMC} of 2036–2617 Ma, suggesting that the Weishan alkaline rocks originated from the lithospheric mantle with the assimilation of crustal material [6,9]. The Guandimiao and Weishan alkaline rocks show a close spatial relationship and crystallization ages, suggesting the magma may have derived from the same source [6,9]. The magma source of the alkaline rocks in the Guandimiao complex originated from the partial melting of lithospheric mantle, which experienced fractional crystallization and crustal contamination processes during its emplacement.

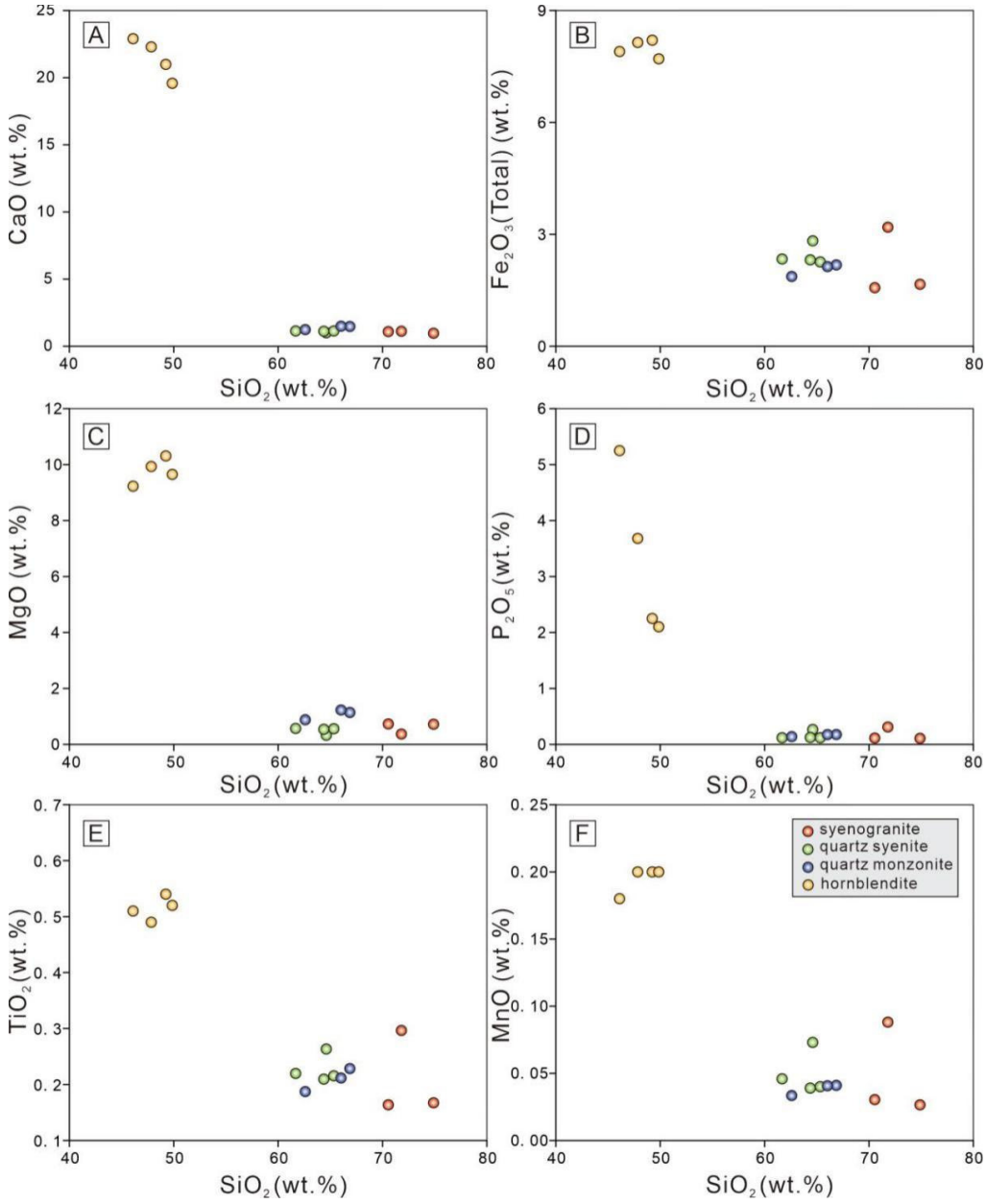

Figure 10. (**A**–**F**) SiO_2 vs. selected major elements showing variable trends for hornblendite, syenogranite, quartz syenite and quartz monzonite [8]. Major elements contents of hornblendite are taken from [7].

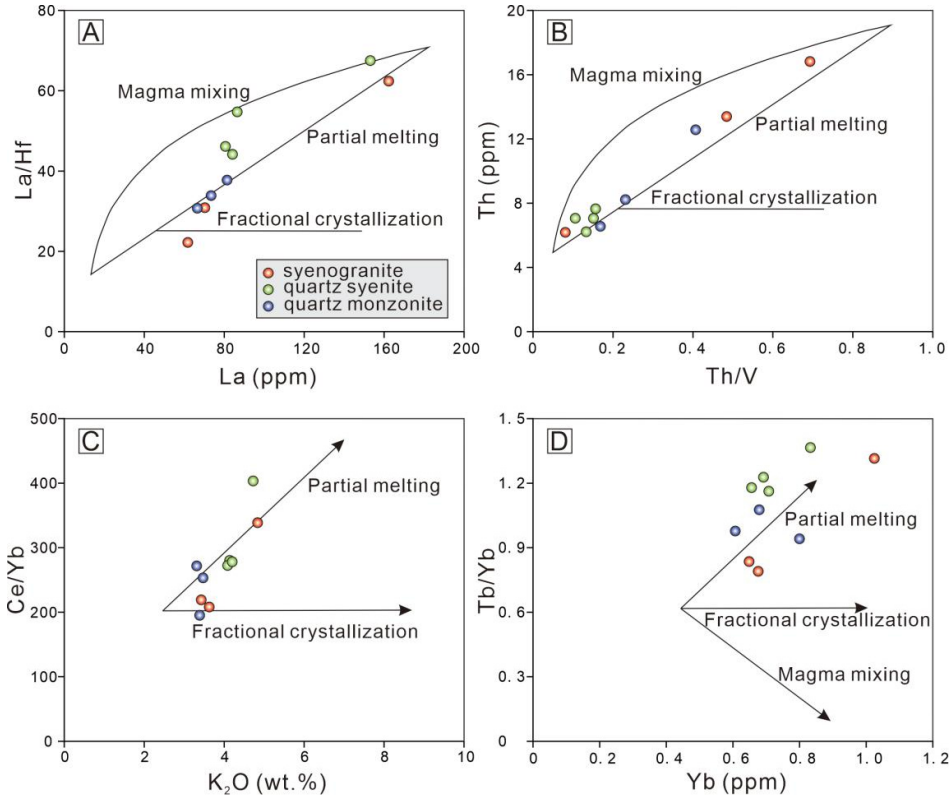

Figure 11. Compositional variation diagrams of (**A**) La/Hf vs. La [45], (**B**) Th vs. Th/V [45], (**C**) Ce/Yb vs. K_2O [21] and (**D**) Tb/Yb vs. Yb [21] for the alkaline rocks showing partial melting.

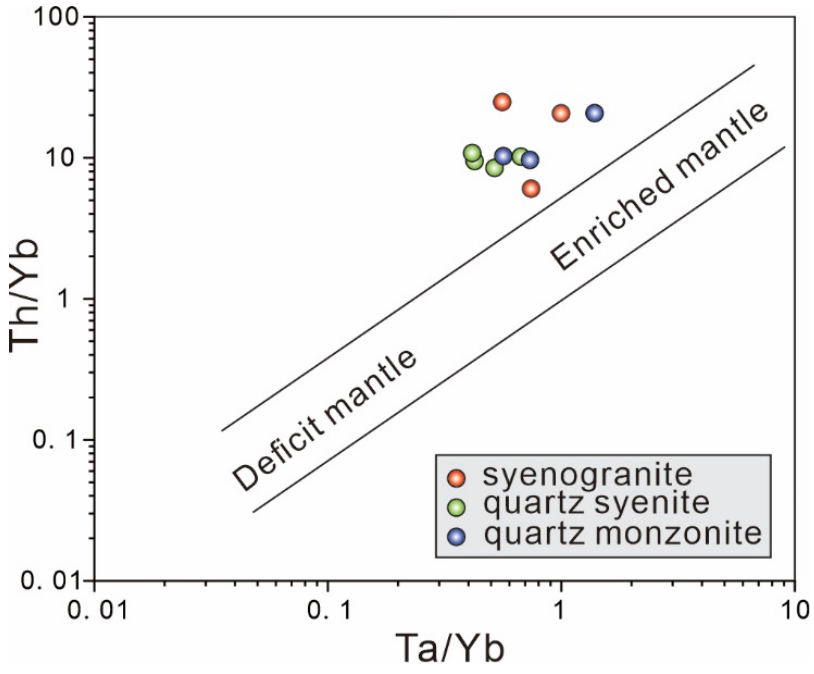

Figure 12. Magma origin discrimination diagram [53].

5.3. Tectonic Implications

The crystallization ages of the alkaline rocks from the Luxi Terrane are in the range of 122–131 Ma, corresponding to the peak time of lithospheric destruction of the NCB (120–130 Ma) [54,55]. In addition, the lithospheric destruction mainly occurred in eastern NCB due to the subduction of the Izanagi plate during the Early Cretaceous [42,56–68].

Hence, the subducting Izanagi plate during the Late Mesozoic may have played an important role in the lithospheric destruction of the NCB. The Izanagi plate subducted beneath the NCB during the Jurassic, resulting in the thickening of the lower crust [60–62]. Asthenosphere upwelling and partial melting of the lithospheric mantle were caused by the rollback of the subducting Izanagi plate during the Early Cretaceous [59,62–66].

The alkaline rocks show enrichment in LREE and LILEs (Rb and Ba), depletion in HREE and HFSEs (Nb, Ta, Ti) characteristics that correspond to volcanic arc granites [42,67–69]. In the tectonic discrimination diagram, the alkaline rocks are mainly plotted in the volcanic arc granites field (Figure 13A–C), which further implies that they were formed in a volcanic arc setting. The alkaline rocks in the Guandimiao complex mainly include syenogranites, quartz syenites and quartz monzonites, which are consistent with active continental margin granites [42]. Furthermore, in the Th/Yb-Yb diagram, the alkaline rocks are mainly plotted in the active continental margin field (Figure 13D) [42]. Hence, the alkaline rocks were probably formed in or near the active continental margin. The active continental margin affinity may be related to the subduction of the Yangtze or Izanagi plate beneath the NCB.

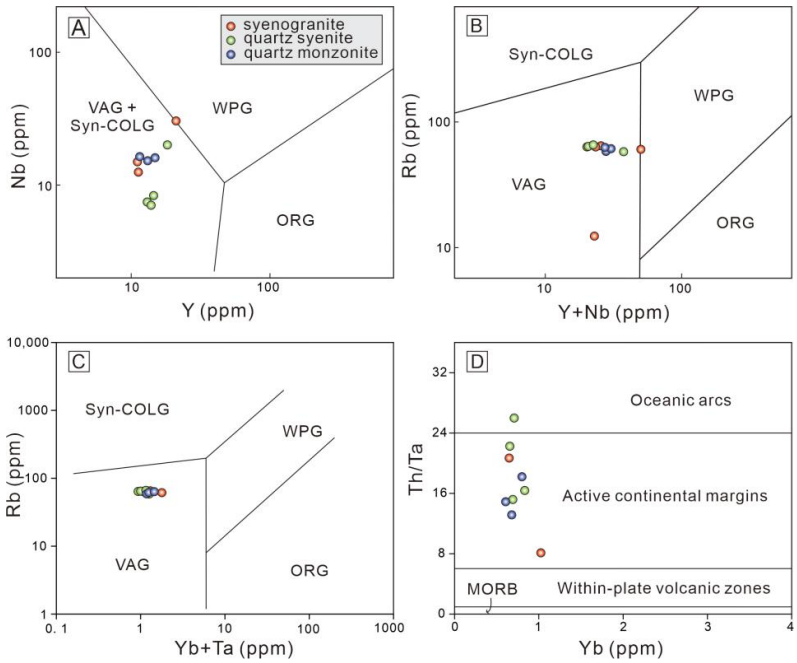

Figure 13. Tectonic implications discrimination diagrams (**A**) Nb vs. Y, (**B**) Rb vs. (Y + Nb) [70], (**C**) Rb vs. (Yb + Ta), (**D**) Th/Ta vs. Yb [48]. Abbreviations: VAG: Volcanic arc granites, Syn-COLG: Syn-collisional granites, WPG: Within plate granites, ORG: Ocean ridge granites.

The alkaline rocks in the Guandimiao complex are alkali and peralkaline, and show high Ga/Al ratios, SiO_2, LREE, Zr and Nb, and low MgO, CaO, Eu contents, which, together with the high abundance of alkali feldspar, are similar to typical A-type granites [42,48,49]. In the tectonic discrimination diagrams (Figure 14), all the alkaline rocks are plotted in the A-type granite field, which further supports that the alkaline rocks are A-type granites. Therefore, the parent magma of the alkaline rocks from the Guandimiao complex is anhydrous, and may have been formed in an anorogenic setting [68]. The alkaline rocks are A-type granites, indicating an extensional decompression process during the magma emplacement [70–74]. Previous studies show that the Izanagi plate subduction might have played an important role in the magmatic activity of the eastern NCB during the Early Cretaceous [69]. Therefore, the alkaline rocks in the Guandimiao complex were probably formed in an extensional back-arc setting induced by the retreat of the subducting Izanagi plate [69,75].

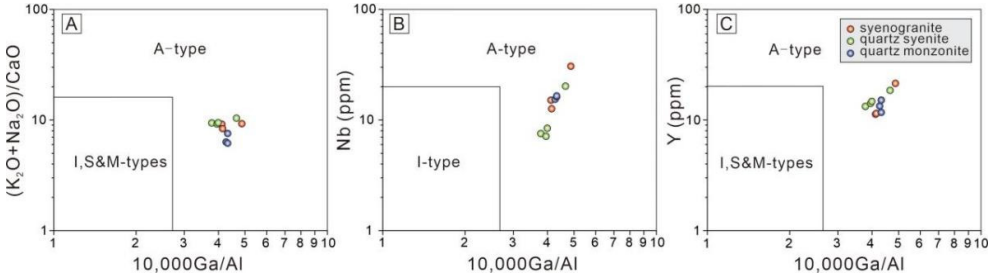

Figure 14. (**A**–**C**) Rock-type discrimination diagrams [46].

In summary, the rollback of the subducting Izanagi plate during the Early Cretaceous triggered the asthenosphere upwelling and lithospheric thinning and partial melting of the lithospheric mantle [76–78]. The lithospheric mantle-derived magma was emplaced at a shallower crustal depth and contaminated by crustal material during ascending, and underwent a fractional crystallization process to form the Guandimiao alkaline rocks (Figure 15).

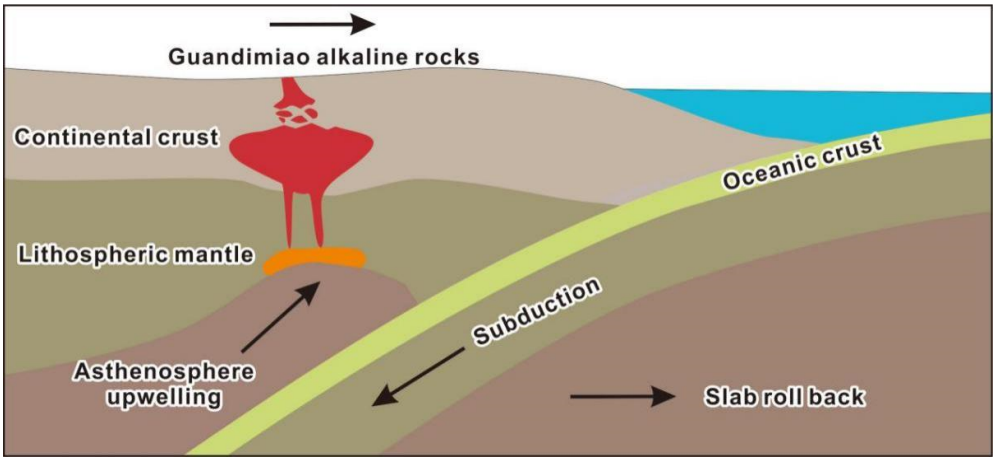

Figure 15. Evolution of the alkaline rocks in the Guandimiao area during the Early Cretaceous [76–78].

6. Conclusions

(1) The sphenes from syenogranite and quartz monzonite show an euhedral–subhedral morphology, which, together with the obvious fractionation between LREE and HREE and high Th/U ratios, imply a magmatic origin.
(2) Sphene U-Pb geochronology indicates that the alkaline rocks in the Guandimiao complex are the products of the Early Cretaceous alkaline magmatism in the Luxi Terrane.
(3) The magma source of the alkaline rocks in the Guandimiao complex originated from the partial melting of lithospheric mantle, which experienced fractional crystallization and crustal contamination processes during its emplacement.
(4) The Guandimiao alkaline complex probably formed in an extensional back-arc setting and the magma upwelling are induced by the retreat of the subducting Izanagi plate.

Author Contributions: Conceptualization: K.-F.Q.; writing: Z.-C.X.; review and editing: C.-L.Z. and Z.S.; formal analysis: S.-S.L. and Y.-Q.H. All authors have read and agreed to the published version of the manuscript.

Funding: This research was funded by the Open Funding of Shandong Provincial Lunan Geology and Exploration Institute (LNY2020-Z02, LNYS202101), the Open Research Project from Key Laboratory of Metallogeny and Mineral Assessment, Institute of Mineral Resources, CAGS (ZS2009), Innovation and Entrepreneurship Training Program of China University of Geosciences, Beijing (S202111415020),

the Beijing Nova Program (Z201100006820097), the 111 Project (BP0719021) and Chinese Postdoctoral Science Foundation (2021M692995).

Acknowledgments: The authors thank Dengyang He for his help in comments.

Conflicts of Interest: The authors declare no conflict of interest.

References

1. Song, M.C.; Yu, X.S.; Song, Y.X.; Xiao, B.J.; Zhou, D.S.; Gao, C.S.; Feng, A.P. Types, sources, and regional crust-mantle evolution background of diamonds in the western Shandong Province. *Acta Geol. Sin.* **2020**, *94*, 2606–2625.
2. Guo, P. Geodynamic Setting of Mesozoic Gold Metallogeny in the Western Shandong Province. Ph.D. Thesis, China University of Geosciences, Beijing, China, May 2014.
3. Goldfarb, R.J.; Mao, J.W.; Qiu, K.F.; Goryachev, N. The great Yanshanian metallogenic event of eastern Asia: Consequences from one hundred million years of plate margin geodynamics. *Gondwana Res.* **2021**, *100*, 223–250. [CrossRef]
4. Lan, T.G.; Fan, H.R.; Hu, F.F.; Yang, K.F.; Wang, Y. Genesis of the Weishan REE deposit, Shandong Province: Evidences from Rb-Sr isochron age, LA-MC-ICPMS Nd isotopic compositions and fluid inclusions. *Geochimica* **2011**, *40*, 428–442.
5. Xie, Y.L.; Xia, J.M.; Cui, K.; Qu, Y.W.; Liang, P.; Zhong, R.C. Rare earth elements deposits in China: Spatio-temporal distribution and ore-forming processes. *Chin. Sci. Bull.* **2020**, *65*, 3794–3808. [CrossRef]
6. Liang, Y.W.; Lai, Y.; Hu, H.; Zhang, F. Zircon U-Pb Ages and Geochemical Characteristics Study of Syenite from Weishan REE Deposit, Western Shandong. *Acta Sci. Nat. Univ. Pekin.* **2017**, *53*, 652–666.
7. Liu, H.; Yu, L.; Chen, H.J.; Qiu, C.G.; Luo, H.D.; Yu, L.S.; Gao, Y.X. Zircon U-Pb Geochronology, Geochemistry and Geological Significance of Guandimiao Complex Intrusion in the East China Craton. *Miner. Depos.* 2022, *in press*.
8. Lan, T.G.; Fan, H.R.; Hu, F.F.; Tomkins, A.G.; Yang, K.F.; Liu, Y.S. Multiple crust-mantle interactions for the destruction of the North China Block: Geochemical and Sr-Nd-Pb-Hf isotopic evidence from the Longbaoshan alkaline complex. *Lithos* **2011**, *122*, 87–106. [CrossRef]
9. Wei, P.F.; Yu, X.F.; Li, D.P.; Liu, Q.; Yu, L.D.; Li, Z.S.; Geng, K.; Zhang, Y.; Sun, Y.Q.; Chi, N.J. Geochemistry, Zircon U-Pb Geochronology, and Lu-Hf Isotopes of the Chishan Alkaline Complex, Western Shandong, China. *Minerals* **2019**, *9*, 293. [CrossRef]
10. Zhi, C.L.; An, M.G.; Huang, K.P.; Shang, Z.; Meng, X.W. Magmatic rock type in Chishan-Longbaoshan area, Shandong Province. Investigation and evaluation design of rare earth mineral resources. 2020; (Unpublished work).
11. Wu, M.Q.; Samon, I.M.; Qiu, K.F.; Zhang, D.H. Multistage metasomatic Zr mineralization in the world-class Baerzhe Rare earth element-Nb-Zr-Be deposit. *Am. Mineral.* **2022**. [CrossRef]
12. Mao, J.W.; Franco, P.; Nigel, C. Mesozoic metallogeny in East China and corresponding geodynamic settings: An introduction to the special issue. *Ore Geol. Rev.* **2011**, *43*, 1–7. [CrossRef]
13. Long, Z.Y.; Qiu, K.F.; Santosh, M.; Yu, H.C.; Jiang, X.Y.; Zou, L.Q.; Tang, D.W. Fingerprinting the metal source and cycling of the world's largest antimony deposit in Xikuangshan, China. *GSA Bull.* 2022; *in press*. [CrossRef]
14. Xu, Y.G.; Huang, X.L.; Ma, J.L. Crust-mantle interaction during the tectono-thermal reactivation of the North China Block: Constraints from SHRIMP zircon U-Pb chronology and geochemistry of Mesozoic plutons from western Shandong. *Contrib. Mineral. Pet.* **2004**, *147*, 750–767. [CrossRef]
15. Wu, M.Q.; Samson, I.M.; Qiu, K.F.; Zhang, D.H. Concentration mechanisms of REE-Nb-Zr-Be mineralization in the Baerzhe deposit, NE China: Insights from textural and chemical features of amphibole and rare-metal minerals. *Econ. Geol.* **2021**, *116*, 651–679. [CrossRef]
16. Hu, Q.Y.; Li, L.; Tang, Z.B.; Shi, X.P. Characteristics and mechanism of Late Mesozoic extensional faults in West Shandong Uplift. *Geol. China* **2009**, *36*, 1233–1244.
17. Li, Y. A Comparative Study of the 1800-1600 Ma Mafic Dike Group in North China: A Case Study of Western Shandon. Master's Thesis, University of Chinese Academy of Sciences, Beijing, China, 2014.
18. Yu, H.C.; Qiu, K.F.; Hetherington, C.J.; Chew, D.; Huang, Y.Q.; He, D.Y.; Geng, J.Z.; Xian, H.Y. Apatite as an alternative petrochronometer to trace the evolution of magmatic systems containing metamict zircon. *Contrib. Mineral. Pet.* **2021**, *176*, 68. [CrossRef]
19. Ma, M.Z.; Wan, Y.S.; Xie, H.Q.; Liu, S.J.; Xie, S.W.; Dong, C.Y.; Bai, W.Q.; Li, Y.; Wang, Y.Q. Neoarchean Mafic Magmatism in Qixingtai Area, West Shandong: Formation Ages and Compositions of Meta-Gabbros. *J. Earth Sci.* **2020**, *45*, 2610–2628.
20. Qiu, K.F.; Yu, H.C.; Deng, J.; McIntire, D.; Gou, Z.Y.; Geng, J.Z.; Chang, Z.S.; Zhu, R.; Li, K.N.; Goldfarb, R. The giant Zaozigou Au-Sb deposit in West Qinling, China: Magmatic- or metamorphic-hydrothermal origin? *Miner. Depos.* **2020**, *18*, 345–362. [CrossRef]
21. Shi, W.J. The Late Mesozoic Tectonic-magematic Evolution Process in the Yishu Fault Zone and Adjacent Regions, Shandong Province: Implication for Gold Mineralization. Ph.D. Thesis, China University of Geosciences, Wuhan, China, May 2014.
22. Qiu, K.F.; Goldfarb, R.J.; Deng, J.; Yu, H.C.; Gou, Z.Y.; Ding, C.J.; Wang, Z.K.; Li, D.P. Gold deposits of the Jiaodong Peninsula, eastern China. *Soc. Econ. Geol. Spec. Publ.* **2020**, *23*, 753–773.
23. Zhao, G.C.; Wilde, S.A.; Cawood, P.A.; Sun, M. Archean blocks and their boundaries in the North China Craton: Lithological, geochemical, structural and P-T path constraints and tectonic evolution. *Precambr. Res.* **2001**, *107*, 45–73. [CrossRef]

24. Zhang, H.F.; Sun, M.; Zhou, X.H.; Ying, J.F. Geochemical constraints on the origin of Mesozoic alkaline intrusive complexes from the North China Craton and tectonic implications. *Lithos* **2005**, *81*, 297–317. [CrossRef]
25. Zhang, S.H.; Zhao, Y.; Li, X.H.; Ernst, R.E.; Yang, Z.Y. The 1.33-1.30 Ga Yanliao large igneous provice in the North China Craton: Implications for reconstruction of the Nuna (Columbia) supercontinent, and specifically with the North Australian Craton. Earth Planet. *Sci. Lett.* **2017**, *465*, 112–125.
26. Rudnick, R.L.; Gao, S.; Ling, W.L.; Liu, Y.S.; Mcdonough, W.F. Petrology and geochemistry of spinel peridotite xenoliths from Hannuoba and Qixia. North China craton. *Lithos* **2004**, *77*, 609–637. [CrossRef]
27. Geng, J.Z.; Qiu, K.F.; Gou, Z.Y.; Yu, H.C. Tectonic regime switchover of Triassic Western Qinling Orogen: Constraints from LA-ICP-MS zircon U-Pb geochronology and Lu-Hf isotope of Dangchuan intrusive complex in Gansu. China. *Geochemistry* **2017**, *77*, 637–651. [CrossRef]
28. Qiu, K.F.; Yu, H.C.; Wu, M.Q.; Geng, J.Z.; Ge, X.K.; Gou, Z.Y.; Taylor, R.D. Discrete Zr and REE mineralization of the Baerzhe rare-metal deposit, China. *Am. Mineral.* **2019**, *104*, 1487–1502. [CrossRef]
29. Liu, Y.S.; Gao, S.; Hu, Z.C.; Gao, C.G.; Zong, K.Q.; Wang, D.B. Continental and oceanic crust recycling-induced melt-peridotite interactions in the Trans-North China Orogen: U-Pb dating, Hf isotopes and trace elements in zircons from mantle xenoliths. *J. Pet.* **2010**, *51*, 537–571. [CrossRef]
30. Ludwig, K.R. *ISOPLOT 3.00: A Geochronological Toolkit for Microsoft Excel*; Berkeley Geochronology Center: Berkeley, CA, USA, 2003; p. 39.
31. Anderson, T. Correction of common lead in U-Pb analyses that do not report 204Pb. *Chem. Geol.* **2002**, *192*, 59–79. [CrossRef]
32. De la Roche, H.; Leterrier, J.; Grandclaude, P.; Marchal, M. A classification of volcanic and plutonic rocks using R1R2-diagram and major-element analyses—Its relationships with current nomenclature. *Chem. Geol.* **1980**, *29*, 183–210. [CrossRef]
33. Frost, B.R.; Barnes, C.G.; Collins, W.J.; Arculus, R.J.; Ellis, D.J.; Frost, C.D. A geochemical classification for granitic rocks. *J. Pet.* **2001**, *42*, 2033–2048. [CrossRef]
34. Frost, C.D.; Frost, B.R. On Ferroan (A-type) Granitoids: Their Compositional Variability and Modes of Origin. *J. Pet.* **2011**, *52*, 39–53. [CrossRef]
35. Shand, S.J. *Eruptive Rocks*; John Wiley and Sons: Hoboken, NJ, USA, 1943; 444p.
36. Sun, S.S.; McDonough, W.F. Chemical and isotopic systematics of oceanic basalts: Implications for mantle composition and processes. *Geol. Soc. Spec. Publ.* **1989**, *42*, 313–345. [CrossRef]
37. McDonough, W.F.; Sun, S. The composition of the Earth. *Chem. Geol.* **1995**, *120*, 223–253. [CrossRef]
38. Pan, H.B.; Kang, Z.Q.; Yang, F.; Fu, W.C. A preliminary study on the paramineralsphene from the subyingan porphyry in Dabaoshan, northern Guangdong. *Geol. Sci. Technol. Inf.* **2014**, *33*, 2014.
39. Deng, X.D.; Li, J.W.; Zhou, M.F.; Zhao, X.F.; Yan, D.R. In-situ LA-ICPMS trace elements and U-Pb analysis of titanite from the Mesozoic Ruanjiawan W-Cu-Mo skarn deposit, Daye district, China. *Ore Geol. Rev.* **2015**, *65*, 990–1004. [CrossRef]
40. Fu, Y.; Sun, X.M.; Lin, H.; Yang, T.J. In-situ LA-ICP-MS U-Pb geochronology and trace elements analysis of polygenetic titanite from the giant Beiya gold-polymetallic deposit in Yunnan Province, Southwest China. *Ore Geol. Rev.* **2016**, *77*, 43–56. [CrossRef]
41. Fu, Y.; Sun, X.M.; Hollings, P.; Li, D.F.; Yang, T.J. Geochronology and trace element geochemistry of titanite in the Machangqing Cu-Mo-dominated polymetallic deposit, Yunnan Province, Southwest China. *J. Asian Earth Sci.* **2018**, *158*, 398–414. [CrossRef]
42. Pearce, J.A.; Harris, N.B.W.; Tindle, A.G. Trace Element Discrimination Diagrams for the Tectonic Interpretation of Granitic Rocks. *J. Pet.* **1984**, *25*, 956–983. [CrossRef]
43. Jin, M.Q.; Li, Y.G.; Wang, P.; Wang, S.S.; Li, W.L. Element fractionation and correction method for U-Pb dating of titanite by laser ablation-inductively coupled plasms-mass spectrometry. *Rock Miner. Anal.* **2020**, *39*, 274–284.
44. Wu, F.Y.; Jahn, B.M.; Wilde, S.A.; Lo, C.H.; Yui, T.F.; Lin, Q.; Ge, W.C.; Sun, D.Y. Highly fractionated I-type granites in NE China (I): Geochronology and petrogenesis. *Lithos* **2003**, *66*, 241–273. [CrossRef]
45. Abdallsamed, M.I.M.; Wu, Y.B.; Zhang, W.X.; Zhou, G.Y. Paleozoic peralkaline A-type magmatism of the Tongbai Orogen, Central China: Petrogenesis and tectonic implications. *Lithos* **2018**, *322*, 268–280. [CrossRef]
46. Xia, L.Q.; Xia, Z.C.; Xu, X.Y.; Li, X.M.; Ma, Z.P. The discrimination between continental basalt and island arc basalt based on geochemical method. *Acta Petrol. Mineral.* **2007**, *26*, 77–89.
47. Barth, M.G.; McDonough, W.F.; Rudnick, R.L. Tracking the budget of Nb and Ta in the continental crust. *Chem. Geol.* **2000**, *165*, 197–213. [CrossRef]
48. Kamber, B.S.; Collerson, K.D. Role of "hidden" deeply subducted slabs in mantle depletion. *Chem. Geol.* **2000**, *166*, 241–254. [CrossRef]
49. Eby, G.N. The A-type granitoids: A review of their occurrence and chemical characteristics and speculations on their petrogenesis. *Lithos* **1990**, *26*, 115–134. [CrossRef]
50. Eby, G.N. Chemical subdivision of A-type granitoids: Petrogenetic and tectonic implications. *Geology* **1992**, *20*, 641–644. [CrossRef]
51. De Paolo, D.J.; Daley, E.E. Neodymium isotopes in basalts of the southwest basin and range and lithospheric thinning during continental extension. *Chem. Geol.* **2000**, *169*, 157–185. [CrossRef]
52. Thomson, R.N.; Morrison, M.A. Asthenospheric and lower lithospheric mantle contributions to continental extentional mgmatism: An example from the British Tertiary Province. *Chem. Geol.* **1988**, *68*, 1–15. [CrossRef]
53. Wilson, M. *Igneous Petrogenesis: A Global Tectonic Approach*; Unwin Hyman: London, UK, 1989; 466p.

54. Minzies, M.A.; Xu, Y.; Zhang, H.; Fan, W. Integration of geology, geophysics and geochemistry: A key to understanding the North China Craton. *Lithos* **2007**, *96*, 1–21. [CrossRef]
55. Zhu, R.; Xu, Y.; Zhu, G.; Zhang, H.; Xia, Q.; Zheng, T. Destruction of the North China Craton. *Sci. China Earth Sci.* **2012**, *55*, 1565–1587. [CrossRef]
56. Pan, F.B.; Liu, R.; Jin, C.; Jia, B.J.; He, X.B.; Gao, Z.; Tao, L.; Zhou, X.C.; Zhang, L.Q. Petrogenesis of Early Cretaceous granitoids from southwest Zhejiang, NE South China Block and its geodynamic implication. *Lithos* **2018**, *308*, 196–212. [CrossRef]
57. Zhang, H.; Sun, M.; Zhou, M.; Fan, W.; Zhou, Z.; Zhai, M. Highly heterogeneous Late Mesozoic lithospheric mantle beneath the North China Craton: Evidence from Sr-Nd-Pb isotopic systematics of mafic igneous rocks. *Geol. Mag.* **2004**, *141*, 55–62.
58. Zhai, M.; Fan, Q.; Zhang, H.; Sui, J.; Shao, J. Lower crustal processes leading to Mesozoic lithospheric thinning beneath eastern North China: Underplating, replacement and delamination. *Lithos* **2007**, *96*, 36–54. [CrossRef]
59. Golonka, J. Phanerozoic Paleoenvironment and Paleolithofacies Maps. Mesozoic. *Geologia* **2007**, *33*, 211–264.
60. Zheng, Y.F.; Xu, Z.; Zhao, Z.F.; Dai, L.Q. Mesozoic mafic magmatism in North China: Implications for thinning and destruction of cratonic lithosphere. *Sci. China Earth Sci.* **2018**, *61*, 353–385. [CrossRef]
61. Zhu, R.X.; Xu, Y.G. The subduction of the west Pacific plate and the destruction of the North China Craton. *Sci. China Earth Sci.* **2019**, *62*, 1340–1350. [CrossRef]
62. Liu, Y.; Wei, J.H.; Zhang, D.H.; Chen, J.J.; Zhang, X.M. Early Cretaceous Wulong intermediate-mafic dike swarms in the Liaodong Peninsula: Implications for rapid lithospheric delamination of the North China Craton. *Lithos* **2020**, *362*, 105473. [CrossRef]
63. Huang, Y.Q.; Wu, M.Q.; Germain, B.; Yu, H.C.; Qiao, B.X.; Zhao, Z.G.; Qiu, K.F. Geodynamic setting and ore formation of the Younusisayi thorium deposit in the Altyn orogenic belt, NW China. *Ore Geol. Rev.* **2021**, *140*, 104552. [CrossRef]
64. Yang, F.; Santosh, M.; Glorie, S.; Jepson, G.; Xue, F.; Kim, S.W. Meso-Cenozoic multiple exhumation in the Shandong Peninsula, eastern North China Craton: Implications for lithospheric destruction. *Lithos* **2020**, *370*, 105597. [CrossRef]
65. Hou, M.L.; Jiang, Y.H.; Jiang, S.Y.; Ling, H.F.; Zhao, K.D. Contrasting origins of late Mesozoic adakitic granitoids from the northwestern Jiaodong Peninsula, East China: Implications for crustal thickening to delamination. *Geol. Mag.* **2007**, *144*, 619–631. [CrossRef]
66. Zhang, H.F.; Sun, M.; Zhou, X.H.; Fan, W.M.; Zhai, M.G.; Yin, J.F. Mesozoic lithosphere destruction beneath the North China Craton: Evidence from major-, trace-element and Sr-Nd-Pb isotope studies of Fangcheng basalts. *Contrib. Mineral. Pet.* **2002**, *144*, 241–254. [CrossRef]
67. Li, S.R.; Santosh, M. Metallogeny and craton destruction: Records from the North China Craton. *Ore Geol. Rev.* **2014**, *56*, 376–414. [CrossRef]
68. Whalen, J.B.; Currie, K.L.; Chappell, B.W. A-Type Granites: Geochemical Characteristics, Discrimination and Petrogenesis. *Contrib. Mineral. Pet.* **1987**, *95*, 407–419. [CrossRef]
69. Ma, Q.; Yang, Y.H.; Zhao, Z.D.; Tong, X.; Wu, J.K.; Miao, Z.; Li, C.; Lei, H.S. Titanite geochronology and geochemistry of the Cenozoic alkali-rich intrusions in the Ailaoshan-Red River Shear Zone, Yunnan Province. *Acta Geol. Sin.* **2020**, *36*, 2751–2764.
70. Samaneh, N.; Karimpour, M.H.; Shafaroudi, A.M.; Santos, J.F.; Mathur, R.; Riibeiro, S. U-Pb geochronology, Sr-Nd isotopic compositions, geochemistry and petrogenesis of Shah Soltan Ali granitoids, Birjand, Eastern Iran. *Geochemistry* **2018**, *78*, 299–313. [CrossRef]
71. Qiu, K.F.; Yu, H.C.; Hetherington, C.; Huang, Y.Q.; Yang, T.; Deng, J. Tourmaline composition and boron isotope signature as a tracer of magmatic-hydrothermal processed. *Am. Mineral.* **2021**, *106*, 1033–1044. [CrossRef]
72. Bonin, B. A-Type Granites and Related Rocks: Evolution of a Concept, Problems and Prospects. *Lithos* **2007**, *97*, 1–29. [CrossRef]
73. Zhu, R.X.; Yang, J.H.; Wu, F.Y. Timing of destruction of the North China Craton. *Lithos* **2012**, *149*, 51–60. [CrossRef]
74. Wang, Y.; Qiu, K.F.; Müller, A.; Hou, Z.L.; Zhu, Z.H.; Yu, H.C. Machine learning prediction of quartz forming-environments. *J. Geophys. Res. Sol. Earth* **2021**, *126*, 1–11. [CrossRef]
75. Maniar, P.D.; Piccoli, P.M. Tectonic discrimination of granitoids. *Geol. Soc. Am. Bull.* **1989**, *101*, 635–643. [CrossRef]
76. Zhu, R.X.; Zhang, H.F.; Zhu, G.; Meng, Q.T.; Fan, H.R.; Yang, J.H.; Wu, F.Y.; Zhang, Z.Y.; Zheng, T.Y. Craton destruction and related resources. *Int. J. Earth Sci.* **2017**, *106*, 2233–2257. [CrossRef]
77. Ma, L.; Jiang, S.Y.; Hou, M.L.; Dai, B.Z.; Jiang, Y.H.; Yang, T.; Zhao, K.D.; Pu, W.; Zhu, Z.Y.; Xu, B. Geochemistry of Early Cretaceous calc-alkaline lamprophyres in the Jiaodong Peninsula: Implication for lithospheric evolution of the eastern North China Craton. *Gondwana Res.* **2014**, *25*, 859–872. [CrossRef]
78. Jiang, Y.H.; Jiang, S.Y.; Ling, H.F.; Ni, P. Petrogenesis and tectonic implications of Late Jurassic shoshonitic lamprophyre dikes from the Liaodong Peninsula, NE China. *Mineral. Pet.* **2010**, *100*, 127–151. [CrossRef]